Desalination and Water Treatment
www.deswater.com

doi: 10.5004/dwt.2023.29509

292 (2023) 216–232
April

Fe-impregnated walnut shell biochars using iron mine tailing wastes as an efficient adsorbent for removal of synthetic dyes

Songhee Baek[a,b], Doyeon Lee[b], Seohyun Ki[b], Woobeom Byeon[b], Yong-Gu Lee[b,c,*], Kangmin Chon[a,b,*]

[a]*Department of Integrated Energy and Infra system, Kangwon National University, 1 Gangwondaehak-gil, Chuncheon-si, Gangwon-do, 24341, Republic of Korea, emails: sbaek.03@gmail.com (S. Baek), kmchon@kangwon.ac.kr (K. Chon)*
[b]*Department of Environmental Engineering, College of Engineering, Kangwon National University, 1 Gangwondaehak-gil, Chuncheon-si, Gangwon-do, 24341, Republic of Korea, emails: sbaek.03@gmail.com (S. Baek), grw06422@naver.com (D. Lee), rltjgus00@naver.com (S. Ki), dnqja8691@naver.com (W. Byeon), yglee19@kangwon.ac.kr (Y.-G. Lee)*
[c]*Institute of Environmental Research, Kangwon National University, 1 Gangwondaehak-gil, Chuncheon-si, Gangwon-do, 24341, Republic of Korea*

Received 3 December 2022; Accepted 29 March 2023

ABSTRACT

In this study, the adsorption of Amaranth (AR) and Fast Green FCF (FG) by walnut shell biochar (WB) and Fe-impregnated WB with iron mine tailing wastes (MWB) was examined to identify the differences in their adsorption mechanisms. The physico-chemical properties of WB and MWB were analyzed using ultra-high-resolution scanning electron microscopy equipped with energy-dispersive X-ray spectroscopy, Fourier-transform infrared spectroscopy, X-ray photoelectron spectroscopy (XPS), and X-ray diffractometer. The adsorption of AR and FG using WB and MWB fit the pseudo-second-order kinetic (R^2: WB = 0.997–0.999, MWB = 0.994–0.998) and Freundlich isotherms (R^2: WB = 0.738–0.927, MWB = 0.983–0.993) better than the pseudo-first-order kinetic (R^2: WB = 0.657–0.969, MWB = 0.982–0.987) and Langmuir isotherms (R^2: WB = 0.711–0.806, MWB = 0.965–0.988). This result suggests that the adsorption of AR and FG onto WB and MWB is governed by chemisorption and multilayer adsorption. Based on the differences in the XPS spectra of WB and MWB before and after the adsorption of AR and FG, the adsorption mechanism of AR and FG onto WB and MWB suggests that the hydrophobic interaction and electrostatic force governs the adsorption of AR and FG. Even following three adsorption–desorption cycles with MeOH, MWB continued to exhibit exceptional reusability (AR = 61.03%, FG = 75.42%). This finding implies that the impregnation of iron materials on the WB surface benefits the adsorption of synthetic dyes in aqueous solutions.

Keywords: Adsorption; Adsorption mechanism; Iron mine tailing; Synthetic dyes; Walnut shells biochar

1. Introduction

The demand for textiles, cosmetics, paper, leather, and pharmaceutical products increased significantly due to rapid economic growth and population expansion that has occurred since the industrial revolution, the amount of synthetic dyes released into the water system is also increasing (3–150,000 tons/y) [1–3]. Approximately 100,000 synthetic dyes are known to be used worldwide, among which azo dyes and triarylmethane dyes are the most widely used [2,4]. Amaranth (AR) is a typical anionic aromatic synthetic dye with one azo bond (–N=N–) that is used for various foods, such as candy, beverages, and caviar, as well as in the textile industry [5,6]. In addition, Fast Green FCF (FG) is one

* Corresponding authors.

of the most representative triarylmethane dyes and is widely used as a colorant for cosmetics, food, and textiles [7,8]. When these synthetic dyes are discharged into the water system, they cause esthetic discomfort and inhibit biological photosynthetic processes in aquatic systems by reducing light transmission [9].

Synthetic dyes generally contain aromatic structures that are not readily biodegradable and therefore are difficult to treat biologically. Thus, various physico-chemical treatments are applied to them, such as coagulation/precipitation, advanced oxidation, membrane, and adsorption processes [10]. The coagulation/precipitation process is the most basic treatment process, in which coagulants are added to wastewater to precipitate and remove dyes, but it has the disadvantage of generating sludge [11]. The advanced oxidation process effectively eliminates the organic compounds by generating radicals with very high oxidizing power, but it has the disadvantage of high operation and management costs [12]. However, the adsorption process is known for its low operating cost and simple design/operation, and it can effectively remove dyes without generating harmful substances and by-products [13,14]. Activated carbon is most commonly used as a representative adsorbent for dye removal owing to its high surface area and adsorption capacity. Still, its application is limited in large-scale treatment facilities because of its high production cost and difficulties in recycling [15]. Accordingly, there is an increasing demand for the development of new adsorbents that are inexpensive and environmentally friendly [16].

Biochar is a carbon-rich material obtained via the pyrolysis of various biomass sources, such as agricultural residues and livestock waste, under the absence of oxygen. It has received great attention as an adsorbent to replace the existing activated carbon because it has a high surface area and porous structure. Biomass can be obtained easily and inexpensively in various places [17]. In addition, the production and use of biochar could contribute to a reduction in global warming by permanently sequestering carbon from the atmosphere [18,19]. Owing to the various oxygen functional groups (e.g., hydroxyl (–OH), carbonyl (–C=O), and carboxyl (–COOH)) present on the surface of biochar, it is effective in removing positively charged organic substances or metal components; meanwhile, it is not effective in removing organic pollutants with relatively negative charged ions. Therefore, various reformation methods have been applied to overcome this limitation [20,21]. Recent studies have demonstrated that biochar composites modified with metals, including iron (Fe), magnesium (Mg), and aluminum (Al), can offer more active adsorption sites and alter the electric charge, enhancing the removal of negative charged organic contaminants [22,23].

5–14 billion tons/y of mine tailings that contain high concentrations of Fe or Al are generated worldwide, which is known to cause severe soil and groundwater contamination when spilled into the environment [24,25]. Elements such as Fe and Al can be used as modifiers to improve the ability of carbon-based adsorbents to remove contaminants. However, few studies have reported using these elements to enhance the performance of biochar [26]. Therefore, modifying biochar using mine tailing waste can be highly useful in manufacturing high-value-added organic adsorbents and simultaneously reducing environmental pollution [27].

The main objective of this study is to estimate the effects of Fe-impregnation using iron mine tailing waste on the synthetic dyes (i.e., AR and FG) removal mechanism of walnut shell biochar. The physico-chemical properties of walnut shell biochar (WB) and Fe-impregnated walnut shell biochar (MWB) were analyzed. In addition, the influence of changes in dosage, pH, temperature, and ionic strength on the AR and FG adsorption using WB and MWB was examined. Furthermore, the adsorption mechanisms of AR and FG by WB and MWB were determined through adsorption kinetics and isothermal experiments.

2. Materials and methods

2.1. Reagents

Walnut shells (WSs) used in this study were obtained from Herb Therapy (Ansan-si, Gyeonggi-do, Republic of Korea), and mine tailing waste was collected from an iron mine located in Jeongseon-gun (Gangwon province, Republic of Korea). AR (85%–95%, $C_{20}H_{11}N_2Na_3O_{10}S_3$) and FG (≥85%, $C_{37}H_{34}N_2O_{10}S_3Na_2$) were purchased from Sigma-Aldrich (St. Louis, MO, USA). The physico-chemical characteristics of AR and FG are shown in Table 1. Sodium hydroxide (98%, NaOH) and hydrochloric acid (35%, HCl) for pH adjustment were purchased from Daejung Chemicals (Sigeng-si, Gyeonggi-do, Republic of Korea).

2.2. Preparation of the WB and MWB

To eliminate impurities, WSs were washed several times using deionized (DI) water and then dried in an oven at 80°C for 24 h. The dried WSs and powdered mine tailings were soaked in a 7.0 N HCl solution (volume = 2.0 L) at a weight ratio of 1:1 (WSs: tailings) for 24 h. After separating the solution using a centrifuge, these pretreated WSs were dried in an 80°C oven for 40 h. The WSs and pretreated WSs with iron mine tailings were pyrolyzed in a tubular furnace (PyroTech, Namyangju, Gyeonggi-do, Republic of Korea) under nonoxygen conditions (atmospheric gas = N_2 (Purity ≥ 99%); flow rate = 0.2 L/min) up to 700°C (heating rate = 10°C/min) for 2 h, and then cooled to room temperature. The prepared WB and MWB samples were rinsed several times with DI water to remove remaining impurities, dried in an 80°C oven for 24 h, homogenized using a 150 μm sieve, and then stored in a desiccator until the experiment.

2.3. Characterization of the WB and MWB

The contents of major elements (C, H, N, O) in WB and MWB were analyzed using the elemental analyzer (Vario MAX cube, Elementar, Langenselbold, Germany). A Brunauer–Emmett–Teller (BET) analyzer (BELSORP-mini II, MicrotracBEL, Osaka, Japan) was used to analyze the surface characteristics of the WB and MWB. The specific surface area and average pore diameter were calculated using the BET equation, and the total pore volume was calculated using the Barrett–Joyner–Halenda method. The surface morphology and composition of WB and MWB were measured using an ultra-high-resolution scanning electron microscopy

Table 1
The physico-chemical properties of Amaranth and Fast Green FCF

Compounds		Amaranth	Fast Green FCF
Formula		$C_{20}H_{11}N_2Na_3O_{10}S_3$	$C_{37}H_{34}N_2Na_2O_{10}S_3$
Structure		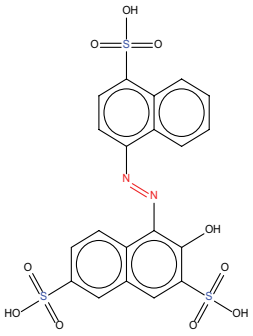	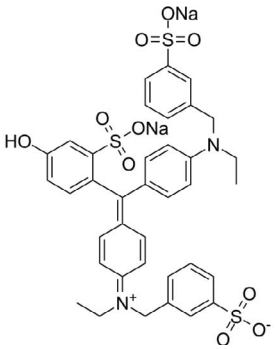
MW (g/mol)		604.47	808.85
Charge[a]	pH 3.0	–3.00	–1.24
	pH 7.0	–3.00	–2.01
	pH 11.0	–3.73	–2.99
log*D*[a]	pH 3.0	–2.88	1.20
	pH 7.0	–2.88	–0.04
	pH 11.0	–3.43	–1.88
pKa[a]		–3.40	–2.40
Water solubility (g/L)[a]		0.028	0.00048

[a]ChemAxon (https://chemicalize.com)

(UHR-SEM; S-4800, Hitachi, Tokyo, Japan) equipped with an energy-dispersive X-ray spectroscopy (EDX) spectrometer. The surface functional groups of WB and MWB were analyzed in the wavelength range of 4,000 to 400 cm^{-1} using Fourier transform-infrared spectroscopy (Frontier Optica, Perkin Elmer, Waltham, MA, USA). The surface composition and surface crystal structure of the WB and MWB were analyzed using X-ray photoelectron spectroscopy (XPS; Nexsa, Thermo Fisher Scientific, USA) and with an X-ray diffractometer (XRD; D/Max-2500, Rigaku, Tokyo, Japan), respectively.

2.4. Batch adsorption experiments

2.4.1. Optimal dosage

To determine the optimal dosage of WB and MWB, the initial concentration of AR and FG solutions was set to 5 mg/L, administering WB and MWB (0.1–2.0 g/L) to the Erlenmeyer flask in which 25 mL of the solution was aliquoted, and then, it was stirred at 150 rpm for 24 h at 25°C using a shaking incubator (VS-8480, Vision Scientific, Daejeon-Si, Republic of Korea). After the adsorption experiment, the solution was filtered using a glass fiber filter (Whatman, Maidstone, UK) with a pore size of 0.7 μm to remove WB and MWB from the solution. The concentrations of AR and FG were analyzed using a UV-Vis spectrophotometer (UV-1280, Shimadzu, Kyoto, Japan) at wavelengths of 520 and 624 nm, respectively [28,29].

2.4.2. Adsorption kinetics experiments

For the adsorption kinetics experiment, the initial concentrations of AR and FG solutions were set to 5 mg/L, administering the optimal dosage of WB and MWB (1.2 g/L) to the Erlenmeyer flask containing 25 mL of solution. It was stirred at 150 rpm for a certain period (0.5–24 h) at 25°C using a shaking incubator. The quantities of AR and FG adsorbed per unit mass of the adsorbent [Q_e (mg/g)] and their removal efficiencies (%) were calculated using the following equations.

$$Q_e = \frac{\left(C_0 - C_e\right)V}{M} \tag{1}$$

$$\text{Removal efficiency}\left(\%\right) = \frac{\left(C_0 - C_e\right)}{C_0} \times 100 \tag{2}$$

where V (L) is the volume of the solution, C_0 and C_e (mg/L) are the concentrations of AR and FG solutions at the initial and equilibrium stages, respectively, and M (g) is the mass of the adsorbent used. The AR and FG kinetics and adsorption capacity by WB and MWB were analyzed using the following equations [30].

$$\text{Pseudo-first-order model: } Q_t = Q_e\left(1 - e^{k_1 t}\right) \tag{3}$$

Pseudo-second-order model: $$Q_t = \frac{Q_e^2 k_2 t}{1 + Q_e k_2 t} \quad (4)$$

Intraparticle diffusion model: $$Q_t = k_{\mathrm{IPD},i} t^{0.5} + C \quad (5)$$

where Q_t (mg/g) is the adsorption capacity at equilibrium, and t (h) is the contact time. k_1 (1/h), k_2 (g/mg·h), and $k_{\mathrm{IPD},i}$ (g/mg·h$^{0.5}$) are the constants of the pseudo-first-order equations, the pseudo-second-order equations, and the intraparticle diffusion rate constants, respectively. The constant C is related to the thickness of the boundary layer [31].

2.4.3. Isothermal adsorption experiments

To understand the isothermal adsorption properties, an experiment was carried out by injecting the optimal dosage of WB and MWB (1.2 g/L) while controlling the initial concentrations of AR and FG solutions (0–3.0 mg/L). It was stirred at 150 rpm for 24 h at 25°C using a shaking incubator to reach the adsorption equilibrium. The isothermal adsorption results were analyzed using the Langmuir isotherm model and the Freundlich isotherm model as follows: [32,33].

Langmuir isotherm: $$Q_e = Q_{\max} \frac{K_L C_e}{1 + K_L C_e} \quad (6)$$

where C_e (mg/L) is the concentration of AR and FG at equilibrium, Q_e (mg/g) is the adsorption capacity at equilibrium (mg/g), and $Q_{\max}$ (mg/g) is the maximum adsorption capacity in the Langmuir isotherm model. K_L (dm^3/mg) is the equilibrium constant of the Langmuir equation, which can be determined through linearization. The adsorption tendency of the Langmuir isotherm model can be determined using the following equation:

$$R_L = \frac{1}{\left(1 + K_L C_0\right)} \quad (7)$$

where R_L and C_0 are the dimensionless separation factor and the initial concentrations of AR and FG, respectively.

Freundlich isotherm model: $$Q_e = K_F C_e^{1/n} \quad (8)$$

where K_F (mg/g)(L/g)^n is the Freundlich adsorption constant, and n is an empirical parameter representing the adsorption strength [34].

2.4.4. Effect of temperature

To understand the effect of the solution temperature on the removal efficiency of AR and FG, adsorption experiments were examined under various temperature conditions (15°C–35°C). Each 25 mL of solution with an initial AR and FG concentration of 5 mg/L was aliquoted into an Erlenmeyer flask, and then, the optimal dosage of adsorbent was added (agitation time = 24 h; agitation speed = 150 rpm). After the adsorption experiment, the adsorbent was removed from the solution in the same manner as previously stated herein. Each experiment was performed three times to minimize errors in measuring residual AR and FG concentrations. The thermodynamic parameters of AR and FG using WB and MWB, such as the free energy change ($\Delta G°$), enthalpy change ($\Delta H°$), and entropy change ($\Delta S°$), were calculated using Eqs. (9)–(11).

$$K_d = \frac{q_e}{C_e} \quad (9)$$

$$\Delta G° = -RT \ln\left(1{,}000 K_d\right) \quad (10)$$

$$\ln\left(1{,}000 K_d\right) = \frac{\Delta S°}{R} - \frac{\Delta H°}{RT} \quad (11)$$

where K_d (dimensionless) is the distribution coefficient, and C_e (mg/L) and q_e (mg/L) are the equilibrium of AR and FG in the liquid phase and at the concentration of AR and FG adsorbed onto WB and MWB at equilibrium, respectively. The unit for $\Delta G°$ is (kJ/mol), for $\Delta S°$ is (J/mol·K), and for $\Delta H°$ is (kJ/mol). R is the ideal gas constant (J/mol·K), and T is the absolute temperature (K). $\Delta H°$ and $\Delta S°$ were the slopes and intercepts of the linear graphs of $\ln K_d$ and $1/T$, respectively [32,33].

2.4.5. Effect of pH

Adsorption experiments were performed by adjusting the initial pH of the AR and FG solutions to 3.0, 5.0, 7.0, and 9.0 to examine the effect of the solution pH on the removal efficiency of AR and FG via the WB and MWB (initial concentration of the AR and FG = 5 mg/L, agitation speed = 150 rpm, temperature = 298 K, adsorbent dosage = 1.2 g/L, and contact time = 24 h). The pH of the solution was adjusted using a 0.1 N HCl solution and 0.1 N NaOH solution.

2.4.6. Effect of ionic strength

To analyze the effect of ionic strength on the removal efficiency of AR and FG using the WB and MWB, adsorption experiments were conducted under various NaCl concentrations (0–0.1 M; initial concentration of the AR and FG = 5 mg/L, agitation speed = 150 rpm, temperature = 298 K, adsorbent dosage = 1.2 g/L, pH = 7.0, and contact time = 24 h).

2.5. Regeneration tests

The reusability of MWB was estimated through three adsorption–desorption cycles in a shaking incubator under constant experimental conditions (initial concentration of each synthetic dye = 5 mg/L, agitation speed = 150 rpm, pH = 7.0, temperature = 25°C, adsorbent dosage = 1.2 g/L, and contact time = 24 h). After each adsorption cycle, MWB with AR and FG was immersed in three distinct desorbents: MeOH, 0.1 M ethylenediaminetetraacetic acid (EDTA), and 0.1 M NaOH (MWB: desorbent ratio = 1:5, w/v), for 24 h, followed by thorough rinsing with DI water. The MWB was then oven-dried for 12 h at 105°C to regenerate it for the next adsorption–desorption cycle. The AR and

FG adsorption efficiencies of MWB from the regeneration experiment were determined using Eq. (2).

3. Results and discussion

3.1. Characterization of WB and MWB

3.1.1. Bulk elemental composition and surface characteristics

Table 2 shows the results of the elemental content and surface characteristic analyses of WB and MWB. Whereas both WB and MWB were found to be mainly composed of carbon, they had a significant difference in the composition ratio; the carbon content was 87.72% for WB, which was reduced to 56.60% for MWB. Conversely, for WB, the ash content was 7.97%, which increased to 35.87% for MWB. This result indicates that through pretreatment, metals, such as Fe, Mg, and Ca, contained in the mine tailings were successfully impregnated onto the surface of the WB. The ratio of H/C, indicating the aromaticity of the adsorbent, was higher for WB (0.32) than for MWB (0.42), which indicates that MWB contains fewer aromatic functional groups. The ratio of O/C, suggesting polarity, was higher for MWB (0.07) than that for WB (0.01), indicating that MWB has more oxygen functional groups and hydrophilic surfaces [35]. In addition, the BET analysis results showed that whereas the average pore size of WB and MWB was the same (WB = 3.41 nm; MWB = 3.41 nm), the specific surface area (WB = 429.94 m^2/g; MWB = 586.62 m^2/g) and total pore volume (WB = 0.08 cm^3/g; MWB = 0.24 cm^3/g) of MWB were increased by 1.4 and 3.0 times, respectively, compared to those of WB. These findings suggest that the Fe component of the mine tailings was successfully impregnated into the surface of WB and that pretreatment using mine tailings can increase the active sites on the surface and improve the physico-chemical properties of WB related to the removal of synthetic dyes [36].

Fig. 1 shows UHR-SEM images of the surfaces of WB (magnification = 2,000) and MWB (magnification = 2,000). The surface of MWB (Fig. 1b) was more irregular and rough than that of WB (Fig. 1a). In addition, the MWB impregnated with Fe had more pores than that of the WB.

Table 2
The physico-chemical properties of WB and MWB

Properties	WB	MWB
C (%)	87.72	56.60
H (%)	2.31	1.99
O (%)	1.54	4.93
N (%)	0.42	0.41
S (%)	0.04	0.20
Ash (%)	7.97	35.87
H/C	0.32	0.42
O/C	0.01	0.07
N/C	0.004	0.006
Specific surface area (m^2/g)	429.94	586.62
Total pore volume (cm^3/g)	0.08	0.24
Average pore size (nm)	3.41	3.41

These results were consistent with the specific surface area analysis result. The ratio of the constituent elements of the WB and MWB examined based on the EDX spectra (Fig. 1c) showed that carbon (C, 96.6 wt.%) and oxygen (O, 3.2 wt.%) were the primary constituent elements of WB. In contrast, MWB contained C (51.8 wt.%), O (21.7 wt.%), and iron (Fe, 22.9 wt.%). The high content of Fe in MWB means that iron mine tailings were successfully impregnated on the surface of WB through pyrolysis and that they played a role in supplementing the surface of the adsorbent with oxygen functional groups [37].

3.1.2. XRD, Fourier-transform infrared spectroscopy, zeta potentials, and XPS analyses

The result of the XRD analysis showed the amorphous carbon (AC) peaks, which are associated with the thermal decomposition of cellulose (the main component of the WSs), shown in Fig. 2a. The AC peaks for WB were observed at 2θ = 23° and 43°, whereas MWB showed peaks associated with Fe_3O_4 (2θ = 18°, 26°, 28°, 30°, 35°, 43°, 50°, 53°, 57°, and 63°) [38,39]. These results imply that the modification method using mine tailings can properly form Fe crystals on the surface of WB, which is in good agreement with the results of EDX analysis. They are consistent with a previous study showing that Fe crystals improve the removal efficiency of anionic contaminants through electrostatic interactions on the adsorbent surface [39]. Fig. 2b reveals the Fourier-transform infrared spectroscopy (FTIR) results of WB and MWB. The FTIR peaks identified in WB were qualified to OH stretching vibrations of alcohols (wavenumbers = 3,650–3,300 cm^{-1}) and C=C stretching vibrations of aromatic rings (wavenumbers = 1,710–1,530 cm^{-1}) [40]. However, the intensities of FTIR peaks representing OH stretching vibrations of alcohols, the C–O–C stretching vibrations of ethers, and Fe–O stretching vibrations (wavenumbers = 670–538 and 524–427 cm^{-1}) were significantly increased. These observations were attributed to the metal oxide that covered the WB surface via Fe-impregnation with iron mine tailings waste [41]. The surface charge characteristics of WB and MWB were analyzed under four different pH conditions (pH = 3, 5, 7, and 9; Fig. 2c). The surface zeta potentials of WB and MWB gradually decreased as the pH increased. The points of zero charge (pH_{PZC}) were 3.99 for WB and 6.04 for MWB, and the difference between these values suggests that electrostatic interactions strongly influence the removal efficiency of anionic synthetic dyes (i.e., AR and FG) on the surfaces of WB and MWB [42]. Fig. 2d–f shows the XPS spectra of WB and MWB. In the C1s XPS spectra, both WB and MWB showed XPS peaks related to the C=C bond of aromatic rings (binding energy = 284.2 eV) and the C–OH bond of alcohols (binding energy = 285.9 eV) [43]. Meanwhile, MWB showed a relatively weak intensity for XPS peaks related to the C=C bond of aromatic rings and the C–OH bond of alcohols, which is considered due to the successful impregnation of the components related to iron oxides on the WB surface [41]. In the O1s XPS spectra, WB showed two relatively weak XPS peaks related to the C=O bond of carbonyls (binding energy = 532.7 eV) and the C–OH bond of alcohols (binding energy = 531.0 eV),

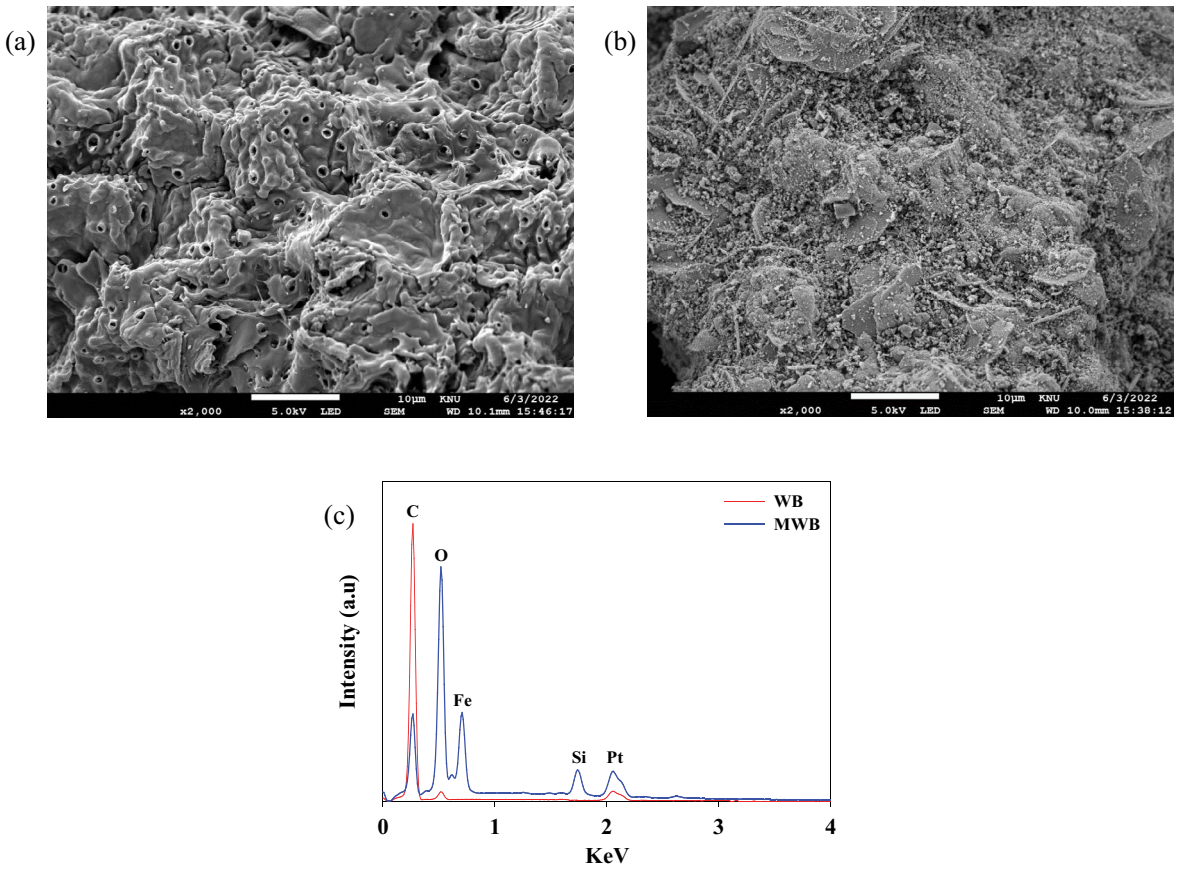

Fig. 1. (a–c) UHR-SEM-EDX images and EDX spectra of WB and MWB.

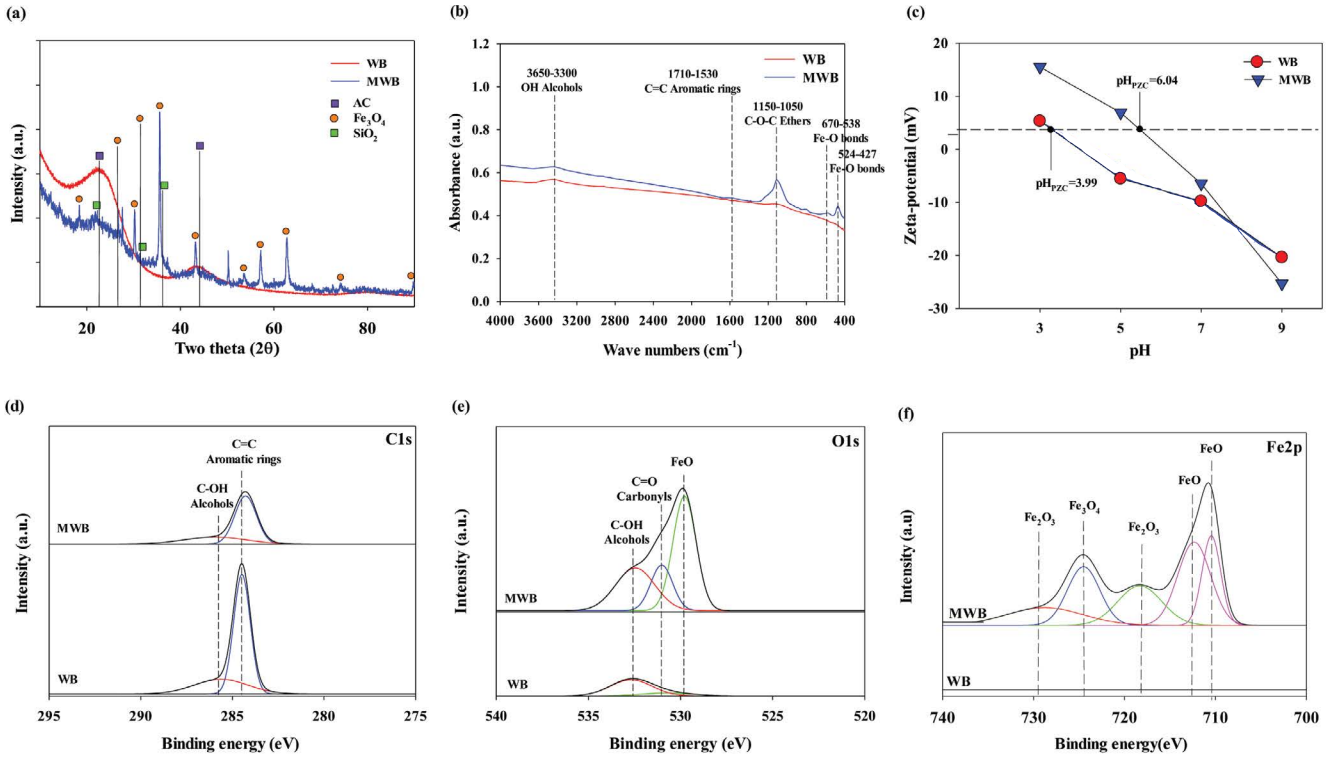

Fig. 2. (a) XRD spectra, (b) FTIR spectra, (c) surface zeta potential, (d) C1s, (e) O1s, and (f) Fe2p XPS spectra of WB and MWB.

whereas MWB showed relatively strong XPS peaks associated with the Fe–O bond of iron oxides (binding energy = 529.8 eV) [44]. In the Fe2p XPS spectra, the XPS peaks were not found in WB, whereas MWB showed those associated with the Fe–O bond of iron oxides (binding energy = 710.5, 712.4 eV), the Fe_2O_3 bond (binding energy = 718.3, 728.8 eV), and the Fe_3O_4 bond (binding energy = 724.5 eV) [44]. These results imply that a high capacity for anion exchange can be imparted through the Fe impregnation of mine tailings on the surface of the WB.

3.2. Effect of optimal dosage of WB and MWB

Fig. 3 shows the removal efficiency of AR and FG depending on the change in the WB and MWB dosage (initial concentration of each synthetic dye = 5 mg/L, agitation speed = 150 rpm, pH = 7.0, temperature = 25°C, adsorbent dosage = 0.1–1.6 g/L, and contact time = 24 h). As the dosage of WB and MWB increased, the removal efficiency of AR and FG increased. This result suggests that the increased dosage

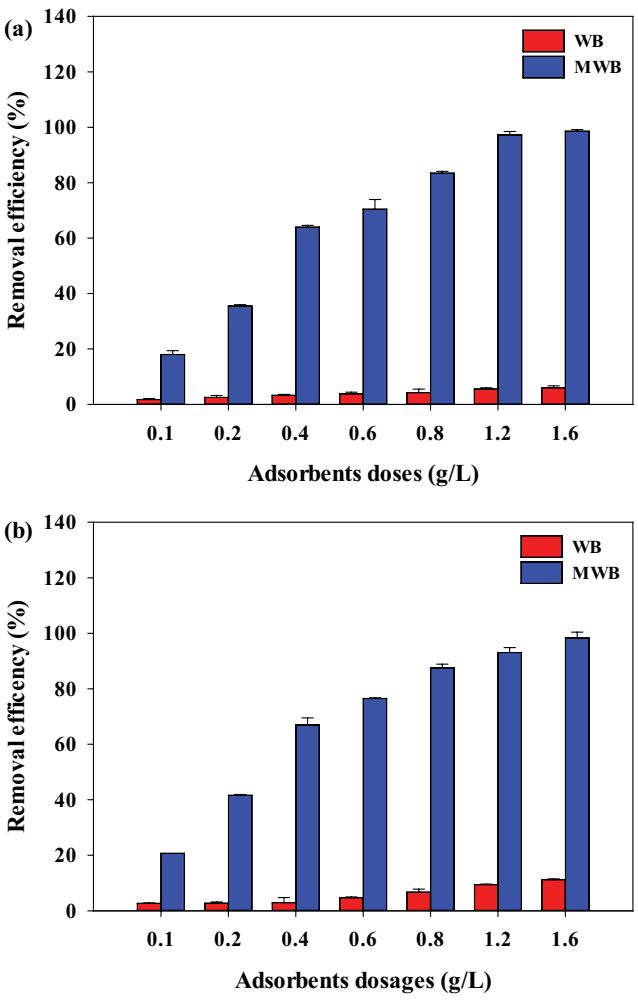

Fig. 3. Effects of adsorbent doses on the adsorptive removal of (a) Amaranth and (b) Fast Green FCF using WB and MWB (initial concentration of each synthetic dye = 5 mg/L, agitation speed = 150 rpm, pH = 7.0, temperature = 25°C, adsorbent dosage = 0.1–1.6 g/L, and contact time = 24 h).

of the adsorbent led to an increase in the surface active sites of WB and MWB, and therefore, the adsorption of AR and FG was facilitated [45]. In an equilibrium state, MWB could adsorb more AR (removal efficiency of MWB = 97%; removal efficiency of WB = 5.5%) and FG (removal efficiency of MWB = 93%; removal efficiency of WB = 9.4%) than that of WB. The reason for this was considered the maximization of the active surface active sites of MWB compared to those of WB through Fe impregnation using mine tailings, which further facilitated adsorption. However, when WB and MWB were administered at >1.2 g/L, the removal efficiency of AR and FG did not increase. These results can be explained by the fact that when more than a certain amount of adsorbent is controlled, the adsorbents aggregate with each other, and the activated portion of the surface decreases [46,47]. In addition, the MWB removed AR more effectively than FG; this was supposed to be because the negative surface charge of AR (charge = −3.7 to −3.0) was greater than that of FG (charge = −2.9 to −1.2) (Table 1). MWB (removal efficiency of AR = 25.5%–98.9%; removal efficiency of FG = 20.7%–98.2%) was found to be more effective than WB (removal efficiency of AR = 1.7%–6.0%; removal efficiency of FG = 2.6%–11.2%) in removing AR and FG. This is because MWB has strong hydrophilicity due to the abundance of oxygen functional groups on the surface (O/C of WB = 0.01; O/C of MWB = 0.07), as well as a high positive charge density owing to Fe impregnation, which enables the effective removal of negatively charged AR and FG. Based on these results, the optimal dosage of WB and MWB was determined to be 1.2 g/L, which was applied to subsequent adsorption experiments.

3.3. Adsorption kinetics experiment

Fig. 4 shows the experimental results of AR and FG adsorption kinetics by WB and MWB. The adsorption of AR and FG by WB and MWB proceeded rapidly but then proceeded slowly after a certain period (≥2 h) as the active part of the surface of WB and MWB became saturated. Equilibrium was reached after 12 h. Table 3 shows the calculated rate constants and correlation coefficients of the adsorption kinetic models. The measured adsorption of AR and FG by WB and MWB was better suited to the pseudo-second-order kinetic model (R^2 of WB: AR = 0.997, FG = 0.999; R^2 of MWB: AR = 0.994, FG = 0.998) than the pseudo-first-order kinetic model (R^2 of WB: AR = 0.969, FG = 0.657; R^2 of MWB: AR = 0.982, FG = 0.987). Accordingly, the adsorption of AR and FG by WB and MWB was considered chemical adsorption by electron exchange or sharing [44]. In addition, the equilibrium adsorption capacity of MWB (Q_e of AR = 4.091 mg/g, Q_e of FG = 3.939 mg/g) was over 10 times higher than that of WB (Q_e of AR = 0.337 mg/g, Q_e of FG = 0.385 mg/g), which means that iron oxides present on the surface of MWB enormously facilitate the adsorption of AR and FG [37]. These results are similar to the equilibrium adsorption capacity of various carbon materials, as shown in Table S1.

The adsorption mechanism for WB and MWB was explained using an intraparticle diffusion model (Fig. 4c–d, Table 4). The adsorption of AR and FG onto WB and MWB in aqueous solution could be divided into three distinct steps

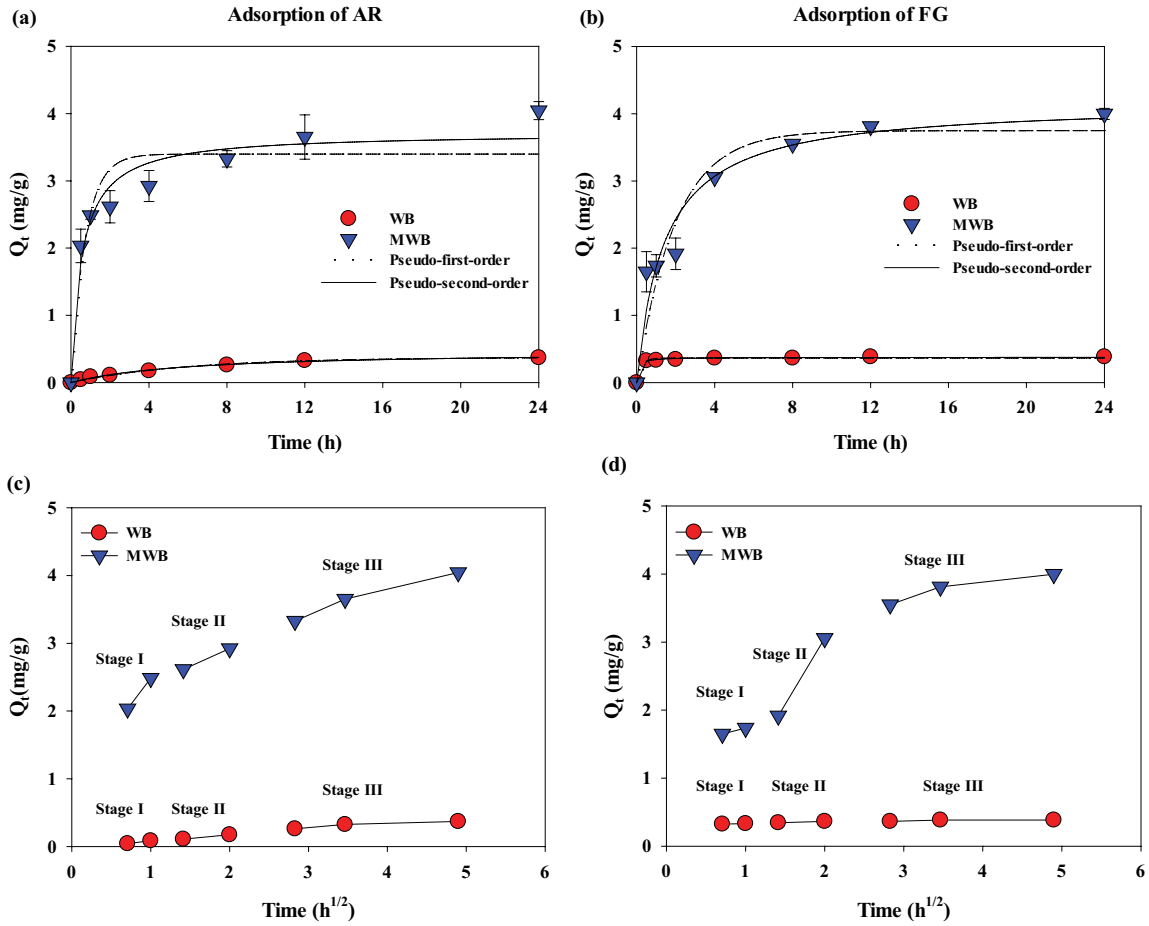

Fig. 4. (a,b) Adsorption kinetics and (c,d) intraparticle diffusion models for the adsorption of Amaranth and Fast Green FCF onto WB and MWB (initial concentration of each synthetic dye = 5 mg/L, agitation speed = 150 rpm, pH = 7.0, temperature = 25°C, contact time = 0–24 h, and adsorbent dosage = 1.2 g/L).

Table 3
Kinetic parameters for the adsorption of Amaranth and Fast Green FCF onto WB and MWB (initial concentration of each synthetic dye = 5 mg/L, agitation speed = 150 rpm, pH = 7.0, temperature = 25°C, contact time = 0–24 h, and adsorbent dosage = 1.2 g/L)

Adsorbents	Compounds	$Q_{e,exp}$ (mg/g)	Pseudo-first-order kinetic model			Pseudo-second-order kinetic model		
			k_1 (1/h)	$Q_{e,cal}$ (mg/g)	R^2	k_2 (g/mg·h)	$Q_{e,cal}$ (mg/g)	R^2
WB	Amaranth	0.337 (±0.036)	0.141 (±0.016)	0.123 (±0.043)	0.969 (±0.003)	3.525 (±0.036)	0.342 (±0.014)	0.997 (±0.004)
	Fast Green FCF	0.385 (±0.025)	4.105 (±0.011)	0.365 (±0.004)	0.657 (±0.008)	7.584 (±0.034)	0.398 (±0.010)	0.999 (±0.002)
MWB	Amaranth	4.091 (±0.014)	0.119 (±0.029)	1.881 (±0.026)	0.982 (±0.009)	0.183 (±0.030)	4.196 (±0.142)	0.994 (±0.001)
	Fast Green FCF	3.939 (±0.014)	4.129 (±0.060)	50.365 (±2.734)	0.987 (±0.005)	0.181 (±0.058)	4.136 (±0.148)	0.998 (±0.002)

as follows: (1) the liquid film diffusion step (reaction time: 0.71–1.00 $h^{0.5}$), where AR ($k_{IPD,1}$ of WB = 1.613 g/mg·$h^{0.5}$; $k_{IPD,1}$ of MWB = 1.117 g/mg·$h^{0.5}$) and FG ($k_{IPD,1}$ of WB = 1.585 g/mg·$h^{0.5}$; $k_{IPD,1}$ of MWB = 0.910 g/mg·$h^{0.5}$) spread rapidly on the outer surface of WB and MWB; (2) the intraparticle diffusion step (reaction time: 1.41–2.00 $h^{0.5}$), where AR ($k_{IPD,2}$ of WB = 1.495 g/mg·$h^{0.5}$; $k_{IPD,2}$ of MWB = 0.778 g/mg·$h^{0.5}$) and FG ($k_{IPD,2}$ of WB = 1.505 g/mg·$h^{0.5}$; $k_{IPD,2}$ of MWB = 1.551 g/mg·$h^{0.5}$) slowly diffused from the outer surface to the inner pores of the WB and MWB; and (3) the adsorption equilibrium step (reaction time: 2.83–4.90 $h^{0.5}$), where AR ($k_{IPD,3}$ of WB = 0.022 g/mg·$h^{0.5}$; $k_{IPD,3}$ of MWB = 0.340 g/mg·$h^{0.5}$) and

FG ($k_{IPD,3}$ of WB = 0.009 g/mg·h$^{0.5}$; $k_{IPD,3}$ of MWB = 0.194 g/mg·h$^{0.5}$) reached adsorption equilibrium as the surface activation fractions of WB and MWB were reduced. Although the adsorption equilibrium step exhibited the lowest k_{IPD} value, it might not be considered a rate-limiting step because it proceeds rapidly [48]. The calculated values of the intraparticle diffusion constant (C) suggested that the liquid film diffusion and intraparticle diffusion steps are the dominant rate-limiting steps in the adsorption of AR and FG by WB and MWB in aqueous solution (WB: C_1 (0.121–0.141) > C_2 (0.114–0.129); MWB: C_2 (0.194–0.900) > C_1 (0.210–0.357)). These findings demonstrated that the presence of positively charged metal species (i.e., Fe) on the MWB surface influences the intraparticle diffusion step, which affects the transport of AR and FG induced by the initial adsorption gradient in aqueous solutions [44].

3.4. Adsorption isotherms and thermodynamics

Table 5 and Fig. 5 show the results of the adsorption isotherms of AR and FG by WB and MWB, using Langmuir and Freundlich isotherm models. The adsorption isotherms of AR and FG by WB and MWB were better suited to the Freundlich isotherm model (WB: R^2 of AR = 0.738, R^2 of FG = 0.927; MWB: R^2 of AR = 0.993, R^2 of FG = 0.983) than to the Langmuir isotherm model (WB: R^2 of AR = 0.711, R^2 of FG = 0.806; MWB: R^2 of AR = 0.988, R^2 of FG = 0.965), indicating that the adsorption of AR and FG by WB and MWB follows a multilayer adsorption process [1]. As a result of evaluating the adsorption tendency of AR and FG by WB and MWB based on the dimensionless adsorption intensity (n), all n values were more significant than 1 at the applied temperature (25°C), showing a favorable adsorption tendency (n > 1: favorable adsorption, n < 1: non-preferential adsorption, n = 1: linear adsorption) [49].

To understand the effect of temperature changes on AR and FG adsorption by WB and MWB, Fig. 6 shows the results of the adsorption experiment performed under three different temperature conditions (15°C–35°C), and Table 6 presents the values of the thermodynamic parameters calculated through this experiment. The removal efficiency of AR and FG by WB and MWB increased as the temperature increased (WB: removal efficiency of AR and FG at 15°C = 1.3%–7.8% → removal efficiency of AR and FG at 35°C = 2.8%–8.2%; MWB: removal efficiency of AR and FG at 15°C = 98.5%–99.5% → removal efficiency of AR and FG at 35°C = 99.6%–100%). The $\Delta G°$ values for AR and FG adsorption using WB and MWB were negative, indicating that the adsorption process proceeded spontaneously [50]. In addition, the $\Delta H°$ values for AR and FG adsorption were positive with both WB and MWB, confirming that AR and FG adsorption toward WB and MWB in aqueous solutions proceeded as endothermic reactions.

3.5. Effects of pH and ionic strength

Fig. 7 shows the effect of the pH (pH = 3–9) on the removal efficiency of AR and FG by WB and MWB.

Table 4
Intraparticle diffusion parameters for the adsorption of Amaranth and Fast Green FCF onto WB and MWB (initial concentration of each synthetic dye = 5 mg/L, agitation speed = 150 rpm, pH = 7.0, temperature = 25°C, contact time = 0–24 h, and adsorbent dosage = 1.2 g/L)

Adsorbents		Stage I			Stage II			Stage III		
		$k_{IPD,1}$ (g/mg·h$^{0.5}$)	C_1 (mg/g)	R^2	$k_{IPD,2}$ (g/mg·h$^{0.5}$)	C_2 (mg/g)	R^2	$k_{IPD,3}$ (g/mg·h$^{0.5}$)	C_3 (mg/g)	R^2
WB	Amaranth	1.613	0.141	1	1.495	0.114	1	0.022	0.231	0.953
	Fast Green FCF	1.585	0.121	1	1.505	0.129	1	0.009	0.254	0.814
MWB	Amaranth	1.117	0.210	1	0.778	0.900	1	0.340	2.430	0.998
	Fast Green FCF	0.910	0.357	1	1.551	0.194	1	0.194	3.007	0.822

Table 5
Isotherm parameters for the adsorption of Amaranth and Fast Green FCF onto WB and MWB (initial concentration of each synthetic dye = 1–10 mg/L, agitation speed = 150 rpm, pH = 7.0, temperature = 25°C, contact time = 24 h, and adsorbent dosage = 1.2 g/L)

Adsorbents	Compounds	Langmuir isotherm model				Freundlich isotherm model		
		Q_{max} (mg/g)	K_L (L/mg)	R_L (mg/L)	R^2	n	K_F [(mg/L)(L/g)$^{1/n}$]	R^2
WB	Amaranth	0.239 (±0.036)	1.113 (±0.516)	0.094 (±0.041)	0.711 (±0.022)	3.945 (±0.671)	0.122 (±0.010)	0.738 (±0.030)
	Fast Green FCF	0.610 (±0.106)	0.542 (±0.264)	0.114 (±0.110)	0.806 (±0.002)	2.602 (±0.384)	0.177 (±0.111)	0.927 (±0.016)
MWB	Amaranth	10.121 (±0.727)	2.748 (±0.497)	0.038 (±0.013)	0.988 (±0.067)	1.957 (±0.190)	7.571 (±0.802)	0.993 (±0.052)
	Fast Green FCF	7.903 (±0.694)	44.539 (±2.062)	0.002 (±0.000)	0.965 (±0.023)	3.642 (±0.067)	11.575 (±0.103)	0.983 (±0.030)

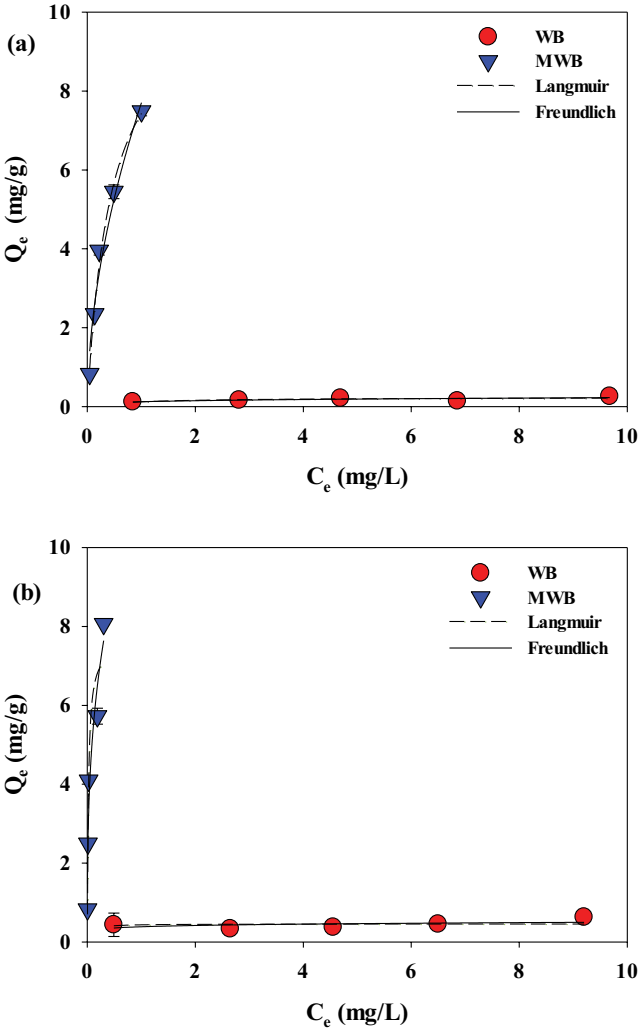

Fig. 5. Adsorption isotherm of (a) Amaranth and (b) Fast Green FCF using WB and MWB (initial concentration of each synthetic dye = 0–10 mg/L, agitation speed = 150 rpm, pH = 7.0, temperature = 25°C, contact time = 24 h, and adsorbent dosage = 1.2 g/L).

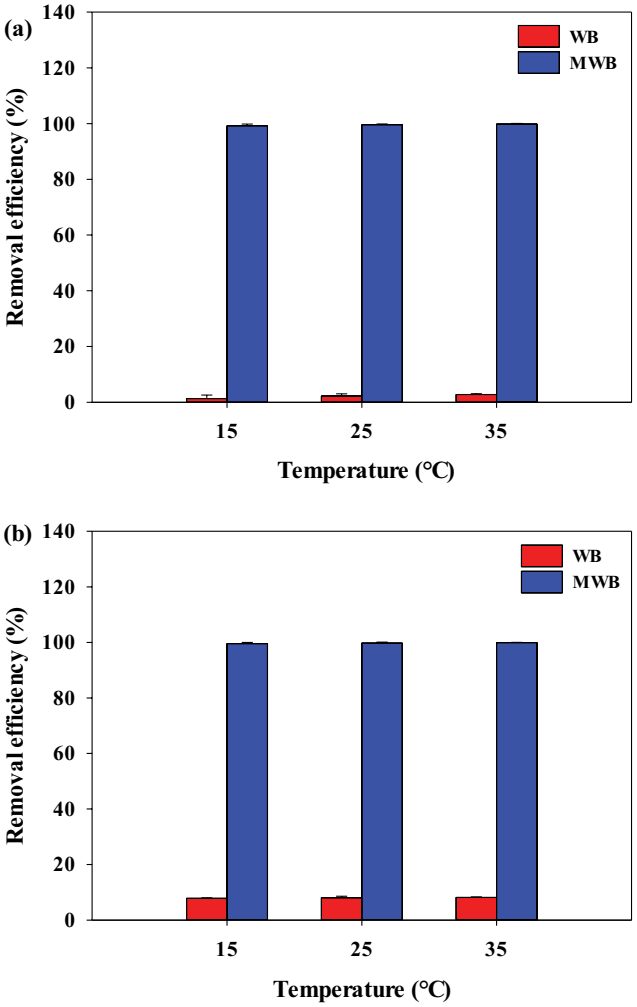

Fig. 6. Effects of temperature on the removal efficiencies of (a) Amaranth and (b) Fast Green FCF using WB and MWB (initial concentration of each synthetic dye = 5 mg/L, agitation speed = 150 rpm, pH = 7.0, temperature =15–25°C, adsorbent dosage = 1.2 g/L, and contact time = 24 h).

The removal efficiency of AR and FG by WB and MWB decreased as the pH increased (AR: removal efficiency of WB = 14.7% (pH 3) → 5.5% (pH 9), the removal efficiency of MWB = 97.6% (pH 3) → 94.2% (pH 9); FG: removal efficiency of WB = 11.8% (pH 3) → 6.0% (pH 9), the removal efficiency of MWB = 99.1% (pH 3) → 93.8% (pH 9)). This result is because the surface charges of WB and MWB become positively charged as the pH of the aqueous solution decreases. Subsequently, the electrostatic attraction for AR and FG (negatively charged on the surface) is strengthened. This is also consistent with the surface zeta potential values of WB and MWB (Fig. 2c).

The effect of ionic strength (ionic strength = 0–0.1 M) on the adsorption of AR and FG by WB and MWB is shown in Fig. 8. The removal efficiencies of AR and FG by WB (removal efficiency of AR = 2.6% (0 M) → 11.5% (0.1 M); removal efficiency of FG = 6.3% (0 M) → 9.2% (0.1 M)) increased with increasing ionic strength, whereas those by MWB (removal efficiency of AR = 98.9% (0 M) → 100% (0.1 M); removal efficiency of FG = 98.4% (0 M) → 100% (0.1 M)) were not significantly affected by the change in ionic strength. These results suggest that the electric double layer on the surface of the adsorbent becomes densified or compressed as the ionic strength increases, leading to the influence of the salt effect, in which the adsorption of anionic compounds by carbon-based adsorbents can be improved [51].

3.6. Adsorption mechanisms

UHR-SEM images before and after adsorption of AR and FG by WB and MWB are presented in Fig. 9. The number of pores in AR and FG-loaded WB and MWB considerably reduced after adsorption, which was distributed to AR and FG inhabiting the WB and MWB surfaces [52]. The XPS spectra of WB and MWB before and after the adsorption of AR and FG are depicted in Fig. 10. After the adsorption of AR and FG, the intensities and positions of the XPS peaks of

Table 6
Thermodynamic parameters for the adsorption of Amaranth and Fast Green FCF using the WB and MWB (initial concentration of each synthetic dye = 5 mg/L, agitation speed = 150 rpm, pH = 7.0, temperature = 15°C–35°C, adsorbent dosage = 1.2 g/L, and contact time = 24 h)

Adsorbents		Thermodynamic parameters			
		Temperature (K)	$\Delta G°$ (kJ/mol)	$\Delta H°$ (kJ/mol)	$\Delta S°$ (J/mol·K)
WB	Amaranth	288	–5.77	0.17	31.26
		298	–7.31		
		308	–8.14		
	Fast Green FCF	288	–10.21	0.01	36.08
		298	–10.63		
		308	–11.03		
MWB	Amaranth	288	–27.04	0.36	115.90
		298	–28.65		
		308	–33.78		
	Fast Green FCF	288	–29.10	0.29	119.97
		298	–31.61		
		308	–34.82		

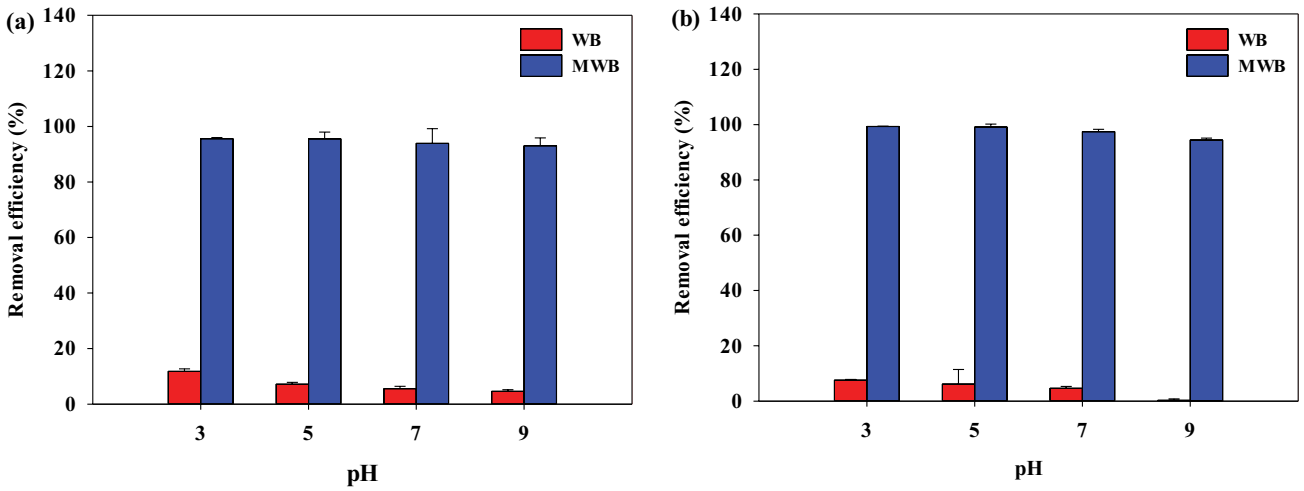

Fig. 7. Effects of the solution pH on the removal efficiencies of (a) Amaranth and (b) Fast Green FCF using WB and MWB (initial concentration of each synthetic dye = 5 mg/L, agitation speed = 150 rpm, pH = 3.0–7.0, temperature = 25°C, adsorbent dosage = 1.2 g/L, and contact time = 24 h).

the C–OH bond of alcohols (binding energy = 285.9 eV) in the C1s spectra of WB and MWB did not change noticeably. However, a significant increase in the intensity of the XPS peak was detected that originated in the C=C bond of aromatic rings (binding energy = 284.2 eV) occurring in WB and MWB after AR and FG adsorption (Fig. 10a and b). In the O1s spectra, the XPS peak intensities assigned to the C–OH bond of alcohols (binding energy = 531.0 eV) did not appear to respond to the adsorption of AR and FG. However, the intensities of the XPS peaks associated with the C=O bond of carbonyls (binding energy = 532.7 eV) and the Fe–O bond of iron oxide (binding energy = 529.8 eV) in the O1s spectra of AR- and FG-loaded WB and MWB were changed considerably compared to those of WB and MWB before the adsorption of AR and FG. These findings were more prominent for AR- and FG-loaded MWB than for AR- and FG-loaded WB. Furthermore, the XPS peak intensity of MWB, indicative of the Fe2p spectra of Fe_2O_3 and Fe_3O_4, substantially decreased after AR and FG adsorption. This observation implies that the electrostatic interaction (e.g., attractions) contributes predominantly to the adsorptive removal of AR and FG via WB and MWB (Fig. 10f) [44]. Based on these findings, the AR and FG adsorption mechanisms onto WB and MWB are proposed as follows: (i) electrostatic attraction between impregnated positively charged iron-oxide groups on the MWB surface and negatively charged synthetic dyes in aqueous solutions mainly governed the adsorption of AR and FG onto MWB, and (ii) hydrophobic interactions played a crucial role in the adsorption of AR and FG using WB [53].

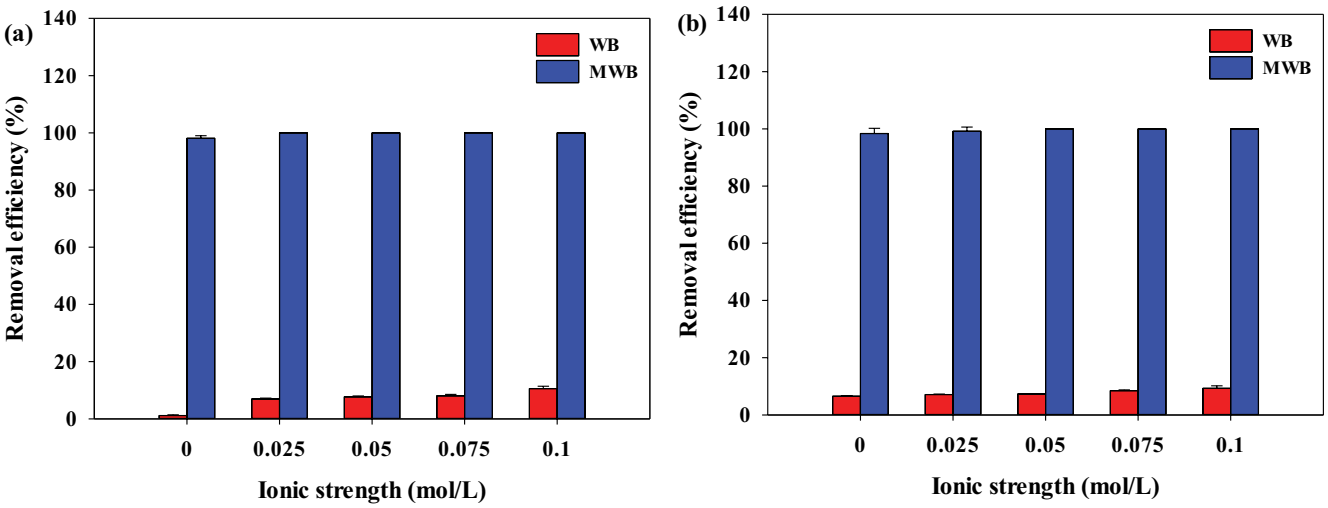

Fig. 8. Effects of the ionic strength on the removal efficiencies of (a) Amaranth and (b) Fast Green FCF using WB and MWB (initial concentration of each synthetic dye = 5 mg/L, agitation speed = 150 rpm, pH = 7.0, temperature = 25°C, adsorbent dosage = 1.2 g/L, and contact time = 24 h).

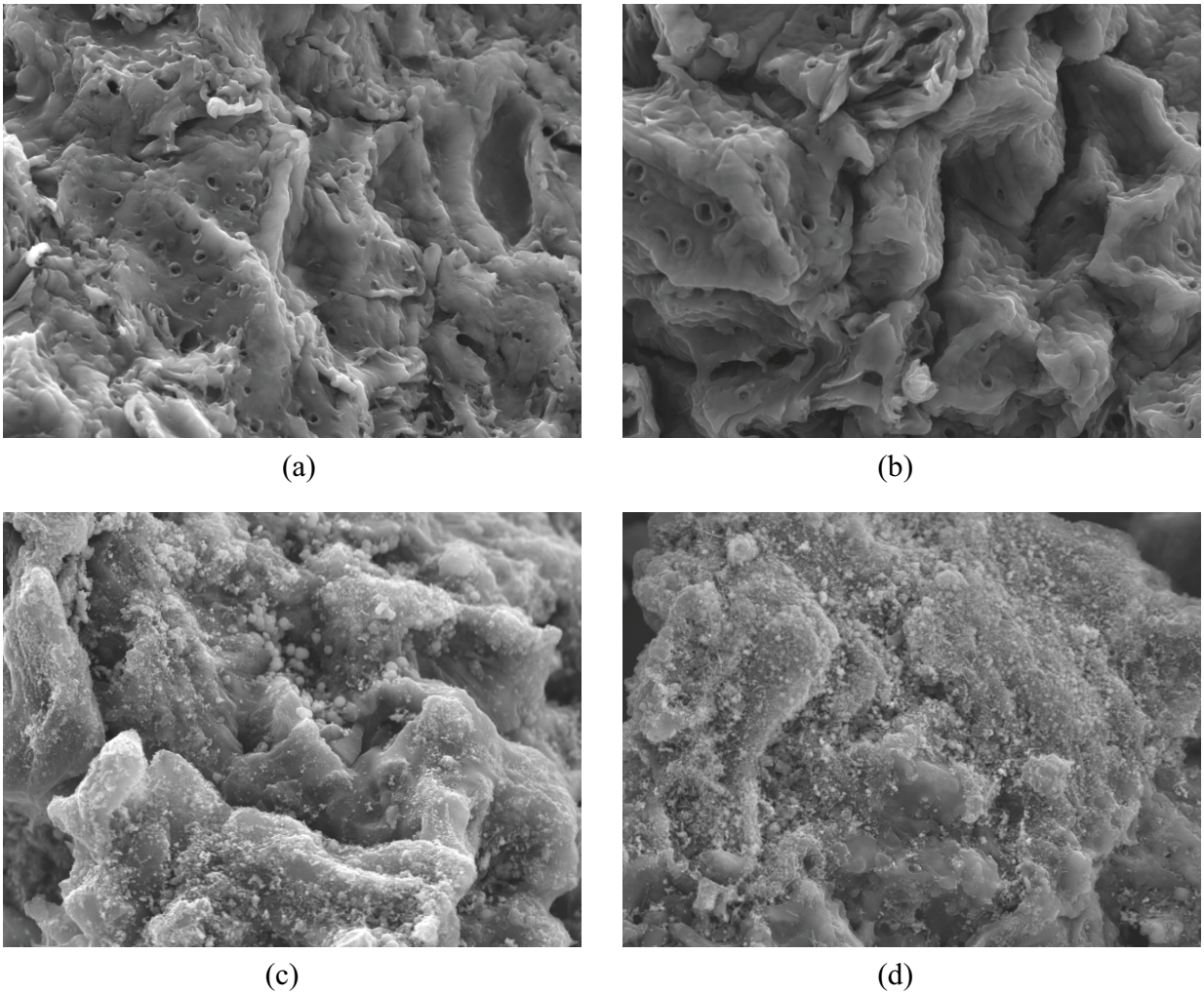

Fig. 9. UHR-SEM images of (a,b) WB and (c,d) MWB before and after the adsorption of Amaranth and Fast Green FCF (magnification = 2,000).

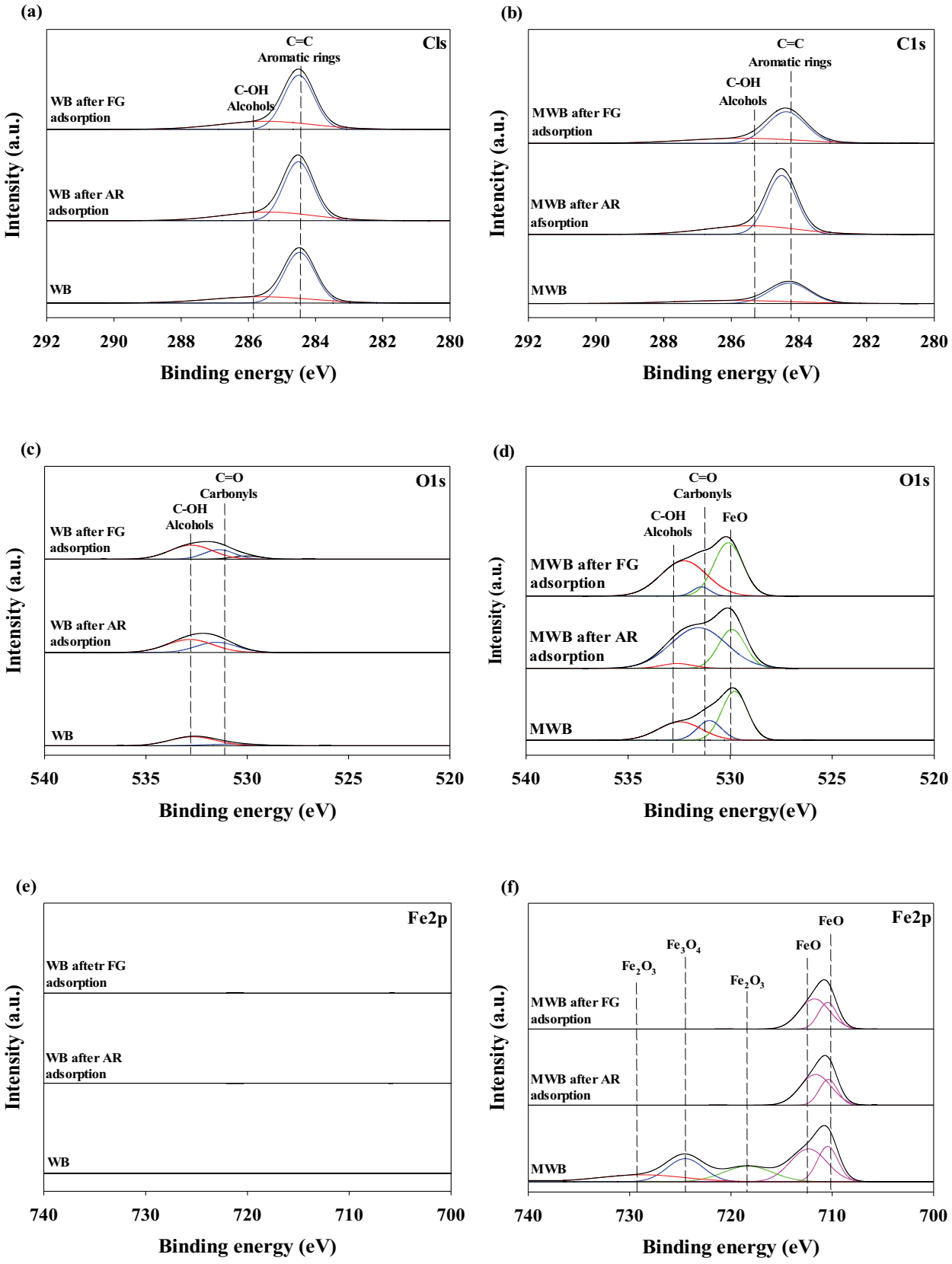

Fig. 10. (a,b) C1s, (c,d) O1s, and (e,f) Fe2p XPS spectra of WB and MWB before and after the adsorption of Amaranth and Fast Green FCF.

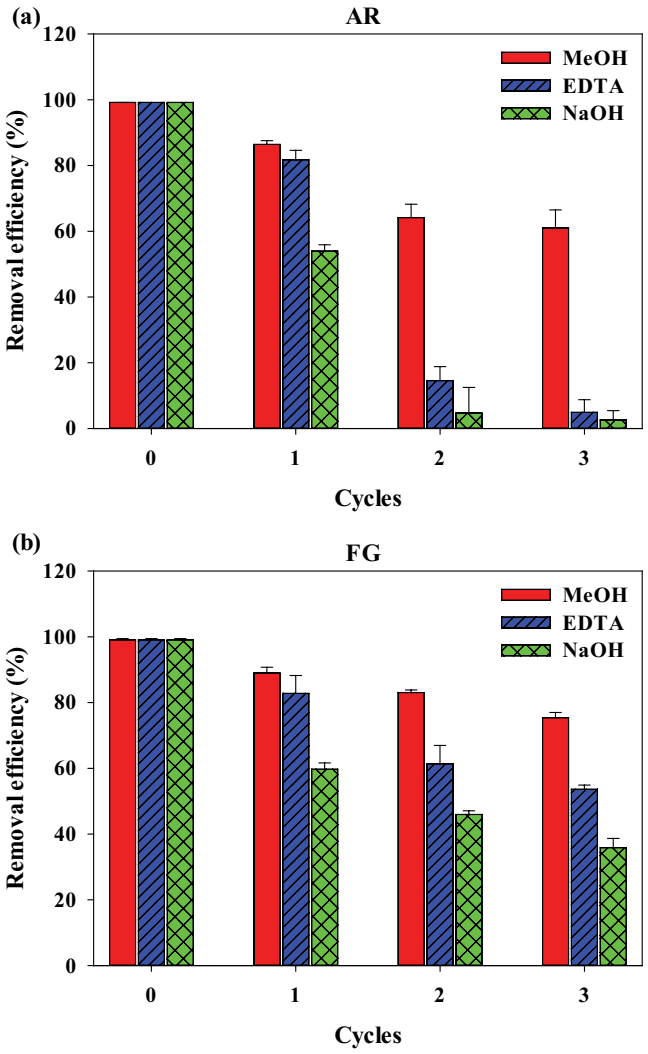

Fig. 11. Reusability efficiencies of MWB with respect to the adsorption of (a) Amaranth and (b) Fast Green FCF using MeOH, 0.1 M EDTA, and 0.1 M NaOH in three adsorption–desorption cycles (initial concentration of each synthetic dye = 5 mg/L, agitation speed = 150 rpm, pH = 7.0, temperature = 25°C, adsorbent dosage = 1.2 g/L, and contact time = 24 h).

3.7. Regeneration of MWB

The reusability of MWB for AR and FG adsorption was evaluated by conducting three adsorption–desorption cycles with three types of desorbents (i.e., MeOH, 0.1 M EDTA, 0.1 M NaOH) (Fig. 11). The removal efficiencies of AR and FG onto MWB progressively declined with each reuse regeneration step. Comparable trends have been observed for pine sawdust biochar with Mg/Al layered double hydroxides and waste coffee residue biochar via magnetization [44,54]. The diminishing removal efficiency of AR and FG toward MWB during successive adsorption–desorption cycles may be attributed to the loss of active adsorption sites due to MWB attrition [44]. Nonetheless, the reuse efficiencies of MWB for AR and FG adsorption persisted after three adsorption–desorption cycles using MeOH (AR = 61.03%, FG = 75.42%), in contrast to 0.1 M EDTA (AR = 4.91%, FG = 53.61%) and 0.1 M NaOH (AR = 2.60%, FG = 35.85%). Consequently, Fe-impregnation could be considered a viable approach to concurrently enhance both the adsorption and desorption capacities of AR and FG on MWB, which can facilitate the reusability in their practical applications for the dyeing wastewater treatment process.

4. Conclusions

This study examined the enhancing synthetic dyes (i.e., AR and FG) adsorption capacity via Fe-impregnation of walnut shell biochar using iron mine tailing wastes. Furthermore, the synthetic dyes adsorption mechanism of WB and MWB was demonstrated through various analytical methods. MWB removed AR (Q_e = 4.091 mg/g) and FG (Q_e = 3.939 mg/g) more than 10 times compared with that of WB (Q_e of AR = 0.337 mg/g and Q_e of FG = 0.385 mg/g) as the Fe-impregnated on the surfaces of WB promoted the adsorptive removal of AR and FG in aqueous solutions. The decreased adsorption of AR and FG onto WB and MWB as increasing pH values may be associated with the increment of electrostatic repulsion. The adsorption of AR and FG using WB and MWB fit the pseudo-second-order kinetic (R^2: WB = 0.997–0.999, MWB = 0.994–0.998) and Freundlich isotherm models (R^2: WB = 0.738–0.927, MWB = 0.983–0.993) better than the pseudo-first-order kinetic (R^2: WB = 0.657–0.969, MWB = 0.982–0.987) and Langmuir isotherm models (R^2: WB = 0.711–0.806, MWB = 0.965–0.988). These results explain that the adsorption of AR and FG onto WB and MWB is principally governed by chemisorption and multilayer adsorption. The liquid film diffusion was the dominant rate-limiting step for the adsorption of AR and FG using WB (C_1 = 0.121–0.141 > C_2 = 0.114–0.129), whereas the intraparticle diffusion was determined to be the rate-limiting step controlling the adsorption of AR and FG onto MWB (C_2 = 0.194–0.900 > C_1 = 0.210–0.357). At the examined temperature range of 288–308 K, the adsorption of AR and FG onto WB (AR: $\Delta G°$ = −8.14 to −5.77 kJ/mol, $\Delta H°$ = 0.17 kJ/mol: FG: $\Delta G°$ = −11.03 to −10.21 kJ/mol, $\Delta H°$ = 0.01 kJ/mol) and MWB (AR: $\Delta G°$ = −33.78 to −27.04 kJ/mol, $\Delta H°$ = 0.36 kJ/mol: FG: $\Delta G°$ = −34.82 to −29.10 kJ/mol, $\Delta H°$ = 0.29 kJ/mol) was endothermic and spontaneous processes. Based on the significant differences in the XPS spectra of WB and MWB before and after the adsorption of AR and FG, the principal adsorption mechanism of AR and FG toward MWB suggests that the electrostatic attraction plays a key role in the adsorption of AR and FG onto MWB between impregnated positively charged iron-oxide groups on the MWB surface and negatively charged synthetic dyes in aqueous solutions. Given that the reusability of MWB for AR and FG adsorption endured after three adsorption–desorption cycles in aqueous solutions (reuse efficiency > 61%), Fe-impregnation may be viewed as a potential technique for enhancing both the adsorption and desorption capacities of AR and FG onto MWB.

Acknowledgment

This work was supported by Korea Environment Industry & Technology Institute (KEITI) through Ecological Imitation-based Environmental Pollution Management

Technology Development Project, funded by Korea Ministry of Environment (MOE)(RE202101286).

References

[1] H. Park, J. Kim, Y.-G. Lee, K. Chon, Enhanced adsorptive removal of dyes using mandarin peel biochars via chemical activation with NH_4Cl and $ZnCl_2$, Water, 13 (2021) 1495, doi: 10.3390/w13111495.

[2] M.T. Yagub, T.K. Sen, S. Afroze, H.M. Ang, Dye and its removal from aqueous solution by adsorption: a review, Adv. Colloid Interface Sci., 209 (2014) 172–184.

[3] O. Anjaneya, S. Shrishailnath, K. Guruprasad, A.S. Nayak, S. Mashetty, T. Karegoudar, Decolourization of Amaranth dye by bacterial biofilm in batch and continuous packed bed bioreactor, Int. Biodeterior. Biodegrad., 79 (2013) 64–72.

[4] E. Forgacs, T. Cserháti, G. Oros, Removal of synthetic dyes from wastewaters: a review, Environ. Int., 30 (2004) 953–971.

[5] S. Shabbir, M. Faheem, N. Ali, P.G. Kerr, Y. Wu, Evaluating role of immobilized periphyton in bioremediation of azo dye Amaranth, Bioresour. Technol., 225 (2017) 395–401.

[6] M. Karkmaz, E. Puzenat, C. Guillard, J. Herrmann, Photocatalytic degradation of the alimentary azo dye Amaranth: mineralization of the azo group to nitrogen, Appl. Catal., B, 51 (2004) 183–194.

[7] W. Przystaś, E. Zabłocka-Godlewska, E. Grabińska-Sota, Biological removal of azo and triphenylmethane dyes and toxicity of process by-products, Water Air Soil Pollut., 223 (2012) 1581–1592.

[8] M. Thakur, G. Sharma, T. Ahamad, A.A. Ghfar, D. Pathania, M. Naushad, Efficient photocatalytic degradation of toxic dyes from aqueous environment using gelatin-Zr(IV) phosphate nanocomposite and its antimicrobial activity, Colloids Surf., B, 157 (2017) 456–463.

[9] N. Mohammadi, H. Khani, V.K. Gupta, E. Amereh, S. Agarwal, Adsorption process of methyl orange dye onto mesoporous carbon material–kinetic and thermodynamic studies, J. Colloid Interface Sci., 362 (2011) 457–462.

[10] A. Mittal, D. Kaur, J. Mittal, Batch and bulk removal of a triarylmethane dye, Fast Green FCF, from wastewater by adsorption over waste materials, J. Hazard. Mater., 163 (2009) 568–577.

[11] V. Golob, A. Vinder, M. Simonič, Efficiency of the coagulation/flocculation method for the treatment of dyebath effluents, Dyes Pigm., 67 (2005) 93–97.

[12] M. Li, Z. Qiang, C. Pulgarin, J. Kiwi, Accelerated methylene blue (MB) degradation by Fenton reagent exposed to UV or VUV/UV light in an innovative micro photo-reactor, Appl. Catal., B, 187 (2016) 83–89.

[13] E. Sharifpour, H.Z. Khafri, M. Ghaedi, A. Asfaram, R. Jannesar, Isotherms and kinetic study of ultrasound-assisted adsorption of malachite green and Pb^{2+} ions from aqueous samples by copper sulfide nanorods loaded on activated carbon: experimental design optimization, Ultrason. Sonochem., 40 (2018) 373–382.

[14] S. Ahad, N. Islam, A. Bashir, S.-u. Rehman, A.H. Pandith, Adsorption studies of Malachite green on 5-sulphosalicylic acid doped tetraethoxysilane (SATEOS) composite material, RSC Adv., 5 (2015) 92788–92798.

[15] J.T. da Fontoura, G.S. Rolim, B. Mella, M. Farenzena, M. Gutterres, Defatted microalgal biomass as biosorbent for the removal of Acid Blue 161 dye from tannery effluent, J. Environ. Chem. Eng., 5 (2017) 5076–5084.

[16] K. Thines, E. Abdullah, N. Mubarak, M. Ruthiraan, Synthesis of magnetic biochar from agricultural waste biomass to enhancing route for wastewater and polymer application: a review, Renewable Sustainable Energy Rev., 67 (2017) 257–276.

[17] J. Yu, X. Zhang, D. Wang, P. Li, Adsorption of methyl orange dye onto biochar adsorbent prepared from chicken manure, Water Sci. Technol., 77 (2018) 1303–1312.

[18] A.A. Abdelhafez, J. Li, Removal of Pb(II) from aqueous solution by using biochars derived from sugar cane bagasse and orange peel, J. Taiwan Inst. Chem. Eng., 61 (2016) 367–375.

[19] S. Jeffery, F.G. Verheijen, M. van der Velde, A.C. Bastos, A quantitative review of the effects of biochar application to soils on crop productivity using meta-analysis, Agric. Ecosyst. Environ., 144 (2011) 175–187.

[20] A. Jahanban-Esfahlan, R. Jahanban-Esfahlan, M. Tabibiazar, L. Roufegarinejad, R. Amarowicz, Recent advances in the use of walnut (*Juglans regia* L.) shell as a valuable plant-based biosorbent for the removal of hazardous materials, RSC Adv., 10 (2020) 7026–7047.

[21] M.E. Mahmoud, A.M. Abdelfattah, R.M. Tharwat, G.M. Nabil, Adsorption of negatively charged food tartrazine and sunset yellow dyes onto positively charged triethylenetetramine biochar: optimization, kinetics and thermodynamic study, J. Mol. Liq., 318 (2020) 114297, doi: 10.1016/j.molliq.2020.114297.

[22] A. Ashiq, B. Sarkar, N. Adassooriya, J. Walpita, A.U. Rajapaksha, Y.S. Ok, M. Vithanage, Sorption process of municipal solid waste biochar-montmorillonite composite for ciprofloxacin removal in aqueous media, Chemosphere, 236 (2019) 124384, doi: 10.1016/j.chemosphere.2019.124384.

[23] Y. Qiu, X. Xu, Z. Xu, J. Liang, Y. Yu, X. Cao, Contribution of different iron species in the iron-biochar composites to sorption and degradation of two dyes with varying properties, Chem. Eng. J., 389 (2020) 124471, doi: 10.1016/j.cej.2020.124471.

[24] J.S. Adiansyah, M. Rosano, S. Vink, G. Keir, A framework for a sustainable approach to mine tailings management: disposal strategies, J. Cleaner Prod., 108 (2015) 1050–1062.

[25] M.O. Mendez, R.M. Maier, Phytostabilization of mine tailings in arid and semiarid environments—an emerging remediation technology, Environ. Health Perspect., 116 (2008) 278–283.

[26] Y. Ahn, D.-W. Cho, W. Ahmad, J. Jo, J. Jurng, M.B. Kurade, B.-H. Jeon, J. Choi, Efficient removal of formaldehyde using metal-biochar derived from acid mine drainage sludge and spent coffee waste, J. Environ. Manage., 298 (2021) 113468, doi: 10.1016/j.jenvman.2021.113468.

[27] N. Araya, A. Kraslawski, L.A. Cisternas, Towards mine tailings valorization: recovery of critical materials from Chilean mine tailings, J. Cleaner Prod., 263 (2020) 121555, doi: 10.1016/j.jclepro.2020.121555.

[28] G. Zhang, Y. Ma, Mechanistic and conformational studies on the interaction of food dye Amaranth with human serum albumin by multispectroscopic methods, Food Chem., 136 (2013) 442–449.

[29] G.A. Epling, C. Lin, Photoassisted bleaching of dyes utilizing TiO_2 and visible light, Chemosphere, 46 (2002) 561–570.

[30] H.N. Tran, S.-J. You, A. Hosseini-Bandegharaei, H.-P. Chao, Mistakes and inconsistencies regarding adsorption of contaminants from aqueous solutions: a critical review, Water Res., 120 (2017) 88–116.

[31] J. Liu, W. Cheng, X. Yang, Y. Bao, Modification of biochar with silicon by one-step sintering and understanding of adsorption mechanism on copper ions, Sci. Total Environ., 704 (2020) 135252, doi: 10.1016/j.scitotenv.2019.135252.

[32] K. Narasimharao, G.K.R. Angaru, Z.H. Momin, S. Al-Thabaiti, M. Mokhtar, A. Alsheshri, S.Y. Alfaifi, J.R. Koduru, Y.-Y. Chang, Orange waste biochar-magnesium silicate (OBMS) composite for enhanced removal of U(VI) ions from aqueous solutions, J. Water Process Eng., 51 (2023) 103359, doi: 10.1016/j.jwpe.2022.103359.

[33] L.P. Lingamdinne, S.K. Godlaveeti, G.K.R. Angaru, Y.-Y. Chang, R.R. Nagireddy, A.R. Somala, J.R. Koduru, Highly efficient surface sequestration of Pb^{2+} and Cr^{3+} from water using a Mn_3O_4 anchored reduced graphene oxide: selective removal of Pb^{2+} from real water, Chemosphere, 299 (2022) 134457, doi: 10.1016/j.chemosphere.2022.134457.

[34] B. Hayati, N.M. Mahmoodi, Modification of activated carbon by the alkaline treatment to remove the dyes from wastewater: mechanism, isotherm and kinetic, Desal. Water Treat., 47 (2012) 322–333.

[35] L. Luo, G. Wang, G. Shi, M. Zhang, J. Zhang, J. He, Y. Xiao, D. Tian, Y. Zhang, S. Deng, The characterization of biochars derived from rice straw and swine manure, and their potential and risk in N and P removal from water, J. Environ. Manage., 245 (2019) 1–7.

[36] R. Zhang, X. Zheng, B. Chen, J. Ma, X. Niu, D. Zhang, Z. Lin, M. Fu, S. Zhou, Enhanced adsorption of sulfamethoxazole from aqueous solution by Fe-impregnated graphited biochar, J. Cleaner Prod., 256 (2020) 120662, doi: 10.1016/j.jclepro.2020.120662.
[37] B. Chen, Z. Chen, S. Lv, A novel magnetic biochar efficiently sorbs organic pollutants and phosphate, Bioresour. Technol., 102 (2011) 716–723.
[38] M. Xie, W. Chen, Z. Xu, S. Zheng, D. Zhu, Adsorption of sulfonamides to demineralized pine wood biochars prepared under different thermochemical conditions, Environ. Pollut., 186 (2014) 187–194.
[39] S. Wang, C. Zhao, R. Shan, Y. Wang, H. Yuan, A novel peat biochar supported catalyst for the transesterification reaction, Energy Convers. Manage., 139 (2017) 89–96.
[40] S. Gupta, G.K. Gupta, M.K. Mondal, Slow pyrolysis of chemically treated walnut shell for valuable products: effect of process parameters and in-depth product analysis, Energy, 181 (2019) 665–676.
[41] M.L. Alvarez, G. Gascó, T. Palacios, J. Paz-Ferreiro, A. Méndez, Fe oxides-biochar composites produced by hydrothermal carbonization and pyrolysis of biomass waste, J. Anal. Appl. Pyrolysis, 151 (2020) 104893, doi: 10.1016/j.jaap.2020.104893.
[42] Y. Zhang, K. Xia, X. Liu, Z. Chen, H. Du, X. Zhang, Synthesis of cationic-modified silica gel and its adsorption properties for anionic dyes, J. Taiwan Inst. Chem. Eng., 102 (2019) 1–8.
[43] S. Li, L. Shao, H. Zhang, P. He, F. Lü, Quantifying the contributions of surface area and redox-active moieties to electron exchange capacities of biochar, J. Hazard. Mater., 394 (2020) 122541, doi: 10.1016/j.jhazmat.2020.122541.
[44] J. Shin, J. Kwak, S. Kim, C. Son, Y.-G. Lee, S. Baek, Y. Park, K.-J. Chae, E. Yang, K. Chon, Facilitated physisorption of ibuprofen on waste coffee residue biochars through simultaneous magnetization and activation in groundwater and lake water: adsorption mechanisms and reusability, J. Environ. Chem. Eng., 10 (2022) 107914, doi: 10.1016/j.jece.2022.107914.
[45] T. Chen, Z. Zhou, R. Han, R. Meng, H. Wang, W. Lu, Adsorption of cadmium by biochar derived from municipal sewage sludge: impact factors and adsorption mechanism, Chemosphere, 134 (2015) 286–293.
[46] S. Banerjee, S. Mukherjee, A. LaminKa-Ot, S. Joshi, T. Mandal, G. Halder, Biosorptive uptake of Fe^{2+}, Cu^{2+} and As^{5+} by activated biochar derived from *Colocasia esculenta*: isotherm, kinetics, thermodynamics, and cost estimation, J. Adv. Res., 7 (2016) 597–610.
[47] S. Mondal, K. Bobde, K. Aikat, G. Halder, Biosorptive uptake of ibuprofen by steam activated biochar derived from mung bean husk: equilibrium, kinetics, thermodynamics, modeling and eco-toxicological studies, J. Environ. Manage., 182 (2016) 581–594.
[48] S. Chen, C. Qin, T. Wang, F. Chen, X. Li, H. Hou, M. Zhou, Study on the adsorption of dyestuffs with different properties by sludge-rice husk biochar: adsorption capacity, isotherm, kinetic, thermodynamics and mechanism, J. Mol. Liq., 285 (2019) 62–74.
[49] K.Y. Foo, B.H. Hameed, Insights into the modeling of adsorption isotherm systems, Chem. Eng. J., 156 (2010) 2–10.
[50] Y.-G. Lee, J. Shin, J. Kwak, S. Kim, C. Son, G.-Y. Kim, C.-H. Lee, K. Chon, Enhanced adsorption capacities of fungicides using peanut shell biochar via successive chemical modification with $KMnO_4$ and KOH, Separations, 8 (2021) 52, doi: 10.3390/separations8040052.
[51] J. Shin, Y.-G. Lee, J. Kwak, S. Kim, S.-H. Lee, Y. Park, S.-D. Lee, K. Chon, Adsorption of radioactive strontium by pristine and magnetic biochars derived from spent coffee grounds, J. Environ. Chem. Eng., 9 (2021) 105119, doi: 10.1016/j.jece.2021.105119.
[52] J. Xie, R. Lin, Z. Liang, Z. Zhao, C. Yang, F. Cui, Effect of cations on the enhanced adsorption of cationic dye in Fe_3O_4-loaded biochar and mechanism, J. Environ. Chem. Eng., 9 (2021) 105744, doi: 10.1016/j.jece.2021.105744.
[53] B. Qiu, Q. Shao, J. Shi, C. Yang, H. Chu, Application of biochar for the adsorption of organic pollutants from wastewater: modification strategies, mechanisms and challenges, Sep. Purif. Technol., 300 (2022) 121925, doi: 10.1016/j.seppur.2022.121925.
[54] J. Kim, G.-H. Bak, D.-Y. Yoo, Y.-I. Lee, Y.-G. Lee, K. Chon, Functionalization of pine sawdust biochars with Mg/Al layered double hydroxides to enhance adsorption capacity of synthetic azo dyes: adsorption mechanisms and reusability, Heliyon, 9 (2023) e14142, doi: 10.1016/j.heliyon.2023.e14142.

Supporting information

Table S1
Comparison of adsorptive removal of Amaranth and Fast Green FCF by various carbon materials

Adsorbents	Dyes	Kinetic model (Q_e, mg/g)	References
NPX nanocomposite hydrogels	Amaranth	Pseudo-second-order (0.36–0.93)	[S1]
Mandarin peel biochar via chemical activation with NH_4Cl and $ZnCl_2$	Fast Green FCF	Pseudo-second-order (0.80–12.45)	[S2]
WB	Amaranth	Pseudo-second-order (0.342)	This study
	Fast Green FCF	Pseudo-second-order (0.398)	
MWB	Amaranth	Pseudo-second-order (4.196)	
	Fast Green FCF	Pseudo-second-order (4.136)	

References

[S1] H. Bai, Q. Zhang, T. He, G. Zheng, G. Zhang, L. Zheng, S. Ma, Adsorption dynamics, diffusion and isotherm models of poly (NIPAm/LMSH) nanocomposite hydrogels for the removal of anionic dye Amaranth from an aqueous solution, Appl. Clay Sci., 124 (2016) 157–166.

[S2] H. Park, J. Kim, Y.-G. Lee, K. Chon, Enhanced adsorptive removal of dyes using mandarin peel biochars via chemical activation with NH_4Cl and $ZnCl_2$, Water, 13 (2021) 1495, doi: 10.3390/w13111495.